Research article

First-principles study of electronic structure and magnetic properties of L1$_0$-ordered FeNi, FePd, and FePt alloys

K. Aledealat [*], B. Aladerah, A. Obeidat, M. Gharaibeh

Physics Department, Jordan University of Science and Technology, Irbid, Jordan

ARTICLE INFO

ABSTRACT

The structural, electronic, and magnetic properties of three spin configurations of L1$_0$-ordered FeM alloys (M = Ni, Pd, or Pt) were studied using the first-principles method. The calculations were carried out using Quantum ESPRESSO package within the framework of Density Functional Theory (DFT). The exchange-correlation functional potentials were studied using local density approximation (LDA) of Perdew-Zunger (PZ), the generalized gradient approximation (GGA) of Perdew–Burke–Ernzerhof (PBE), Perdew and Wang 91 (PW91), and Perdew-Burke-Ernzerhof revised for solids (PBEsol). We found that the PBE approximation has the most accurate results for lattice parameters compared to the experimental values. Furthermore, our results reveal that the most stable spin configuration for the considered alloys is the ferromagnetic configuration, where all spins are aligned perpendicular to the (001) plane. However, in FePd and FePt alloys, a small variation in the tetragonality ratio c/a (from 0.98 to 0.92) can transform them from ferromagnetic to antiferromagnetic state. In an antiferromagnetic state, a pseudogap is observed just below fermi energy for each alloy. Moreover, our calculations reveal large magnetocrystalline anisotropies for FePt alloy in the order of 3 meV/f.u. On the other hand, FePd and FeNi show relatively lower values in the range of 0.18–0.42 meV/f.u. Finally, Heisenberg exchange interactions are calculated from first-principles and Green's functions formalism.

1. Introduction

In the last decade, transition metal alloys were the focus of numerous studies in the last decade due to their potential applications in many fields. These applications include magneto-optical recording technologies [1, 2, 3], magnetic media [4], magnetic sensors [5, 6], and catalytic applications [7, 8, 9]. The main attraction forms of these alloys are nanoparticles and thin films [10, 11]. The key factor for these alloys is their divers' magnetic properties and the ability to control their parameters by adjusting their growth formula and conditions. For instance, if these alloys are engineered to have large saturation magnetization (Ms), high Curie temperature (T$_C$), and large magnetocrystalline anisotropy energy (MCA), then they can be employed in many technological applications such as electric motors and storage devices [12].

Magnetocrystalline anisotropy energy is the difference in the total energy for spin moment alignment along different crystallographic axes, typically termed an easy and a hard axis. It originates from spin-orbit interactions, which are considered short-range interactions [13, 14, 15]. For example, it has been shown that the MCA for FePt alloy can be substantially increased up to the order of 10 MJ/m^3 [16, 17, 18, 19, 20] when it is

in the L1$_0$ ordered phase. Similarly, FePd [21, 22] and FeNi [14, 23, 24] alloys in the L1$_0$ ordered phase showed relatively high MCA values.

According to work done by Brown *et al.* on FePt alloys in the L1$_0$ phase. [25], strong competition is present between ferromagnetism (FM) and antiferromagnetism (AFM) states. Their results reveal that the FM state is more favorable as tetragonal distortion decreases. Shuttleworth [26] employed spin-polarized density functional theory (DFT) to study the band structure of binary Pt$_x$M$_{1-x}$ (M = Fe, Co, and Ni) alloys in the ordered L1$_2$ and L1$_0$ phases.

Werwiński *et al.* [27] calculated MCA for L1$_0$ FeNi using generalized gradient approximation (GGA) with WIEN2K, FLPO, and FP-SPR-KKR code. The estimated value is less than 0.5 MJ m^{-3} which is below the reported values in the literature. This expected limitation in the GGA result can be improved by including additional factors such as tetragonal strain and alloying [27]. Burzo *et al.* [28] studied band structure and magnetic properties of FePd ordered compounds using first-principles calculations. Their calculations for magnetic moments are in very good agreement with the reported experimental values.

In this work, structural, electronic, and magnetic properties of L1$_0$-ordered binary FeNi, FePd, and FePt alloys are investigated using several

---

* Corresponding author.
  E-mail address: kmaledealat@just.edu.jo (K. Aledealat).

exchange-correlation approximations. This work includes calculating Lattice parameters, bulk modulus, the total and partial density of states, total and partial magnetic moment, magnetocrystalline anisotropy, Hubbard parameter, and Heisenberg exchanges interactions. The achieved results are discussed and compared to the available experimental and theoretical values.

1.1. Computational method

Fully L1$_0$-ordered FeNi, FePd, and FePt alloys were considered in three collinear spin configurations: antiferromagnetic (AFM), ferrimagnetic (FIM), and ferromagnetic (FM), as shown in Figures 1 and 2. Quantum ESPRESSO [29, 30] was used for spin density functional calculations. The

Projector Augmented Wave method (PAW) [31, 32, 33] was utilized to describe electron-ion interactions where the valence electron configurations for iron, nickel, palladium, and Platinum are, respectively, as follows: $3d^6 4s^2$, $3d^8 4s^2$, $4d^{10}$, $5d^9 6s^1$. The exchange-correlation functional potentials were studied using: local density approximation (LDA) of Perdew-Zunger (PZ) [34], the generalized gradient approximation (GGA) of Perdew–Burke–Ernzerhof (PBE) [35, 36], Perdew and Wang 91 (PW91) [36], and Perdew-Burke-Ernzerhof revised for solids (PBEsol) [37].

A wave-function kinetic energy cutoff of 75 Ry, a charge density cutoff of 500 Ry, and a first-order Methfessel–Paxton smearing of 0.02 Ry were used throughout this work. In addition, a low value of mixing parameter (0.05) was used to ensure convergence of the self-consistent field to the lowest Kohn–Sham energy state.
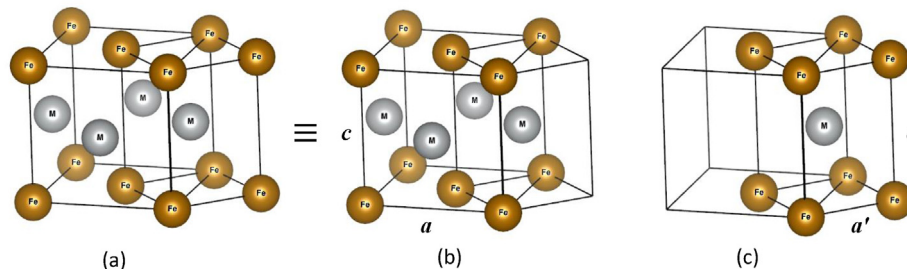

Figure 1. (a) L1$_0$ structure of FeM (M = Ni, Pd, or Pt) consist of two possible unit cells (b) Schematic diagram of FCT unit cell (c) Schematic diagram of BCT unit cell.
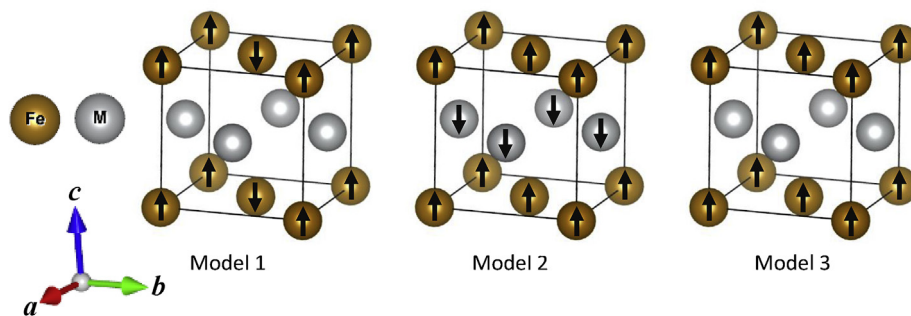

Figure 2. Antiferromagnetic (Model 1), ferrimagnetic (Model 2), and ferromagnetic (Model 3) configurations of fully L1$_0$-ordered FeM (M = Ni, Pd, or Pt) alloys.

Table 1. The lattice parameters (a and c) and the bulk modulus for FeM (M = Ni, Pd, or Pt) calculated for the configurations illustrated in Figure 2.

Cal. Method	a (Å)				c (Å)				B (GPa)	dB
	PZ	PBE	PBEsol	PW91	PZ	PBE	PBEsol	PW91	PBE	PBE
FeNi										
Model 1	3.41	3.55	3.49	3.55	3.41	3.55	3.49	3.55	164.7	5.96
Model 2	3.43	3.57	3.48	3.54	3.43	3.57	3.47	3.59	172.4	5.57
Model 3	3.47	3.57	3.49	3.55	3.47	3.57	3.56	3.62	182.5	5.43
Theor.	3.56 [27]				3.58 [27]				194	
Exp.	3.57 [44]				3.57 [44]				165–177	-
FePd										
Model 1	3.78	3.94	3.86	3.92	3.63	3.63	3.55	3.60	145.4	4.81
Model 2	3.78	3.86	3.83	3.87	3.65	3.78	3.75	3.78	151.4	5.29
Model 3	3.76	3.84	3.78	3.84	3.68	3.76	3.71	3.76	159.2	5.04
Theor	3.80 [28]				3.66 [28]				-	-
Exp.	3.855 [45]				3.714 [45]				-	-
FePt										
Model 1	3.81	3.92	3.89	3.92	3.58	3.60	3.58	3.60	180	5.02
Model 2	3.83	3.86	3.92	3.87	3.62	3.76	3.65	3.59	186.7	5.21
Model 3	3.76	3.86	3.81	3.86	3.68	3.79	3.73	3.79	194.8	5.07
Theor	3.89 [26]				3.705 [26]				-	-
Exp.	3.85 [46], 3.86 [47]				3.713 [46], 3.79 [47]				-	-

Table 2. The total energy difference between the three considered models and the calculated Hubbard effective parameters for each atomic type.

Alloy	Model	ΔE (mRy)	U_{Fe} (eV)	U_M (eV)
FeNi	Model 1	46.97	1.404	2.783
	Model 2	5.37		
	Model 3	0.0		
FePd	Model 1	59.48	1.905	0.062
	Model 2	3.82		
	Model 3	0.0		
FePt	Model 1	62.58	1.671	0.147
	Model 2	9.34		
	Model 3	0.0		

The equilibrium lattice parameters a_0 presented in Table 1 for L1$_0$ structures were obtained by letting the lattice to relax along the c direction for each value of a. Then, the equation of state for each alloy was calculated and numerically minimized. Finally, the equation of state was obtained by plotting the density functional theory (DFT) Kohn–Sham energy as a function of volume. The achieved equilibrium lattice parameters with this approach were used throughout the remainder of this work.

For MCA calculation, the spin-orbit coupling included in Kohn–Sham equation was employed in the force theorem to get more accurate results. Two sets of self-consistent field calculations were performed for each alignment of the magnetic moment. One oriented parallel to the easy axis (c-axis) yields the energy E_{II} and the other aligned perpendicular to the easy axis yields the energy $E_\perp$. Thus, the MCA can be given by the following equation.

$$MCA = E_{II} - E_\perp$$

Furthermore, The Dudarev [38] approach was applied where we considered only Hubbard effective parameter $U_{eff} = U - J$, here U and J are Coulomb and exchange parameters, respectively. J is considered zero. Hence, U_{eff} is equal to U in our calculations. The values of this parameter
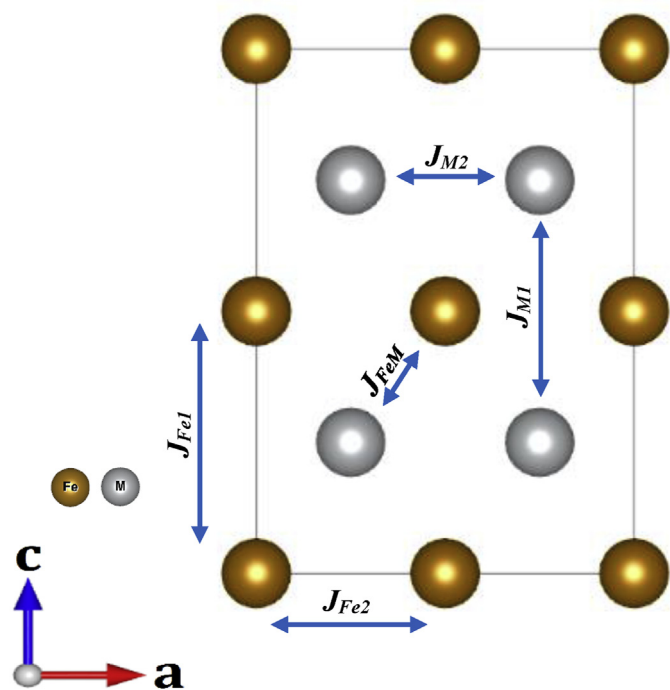

Figure 3. Schematic view of FeM (M = Ni, Pd, or Pt) supercell. Five types of Heisenberg exchange interactions between Fe–Fe, Fe-M, and M-M atoms are shown.
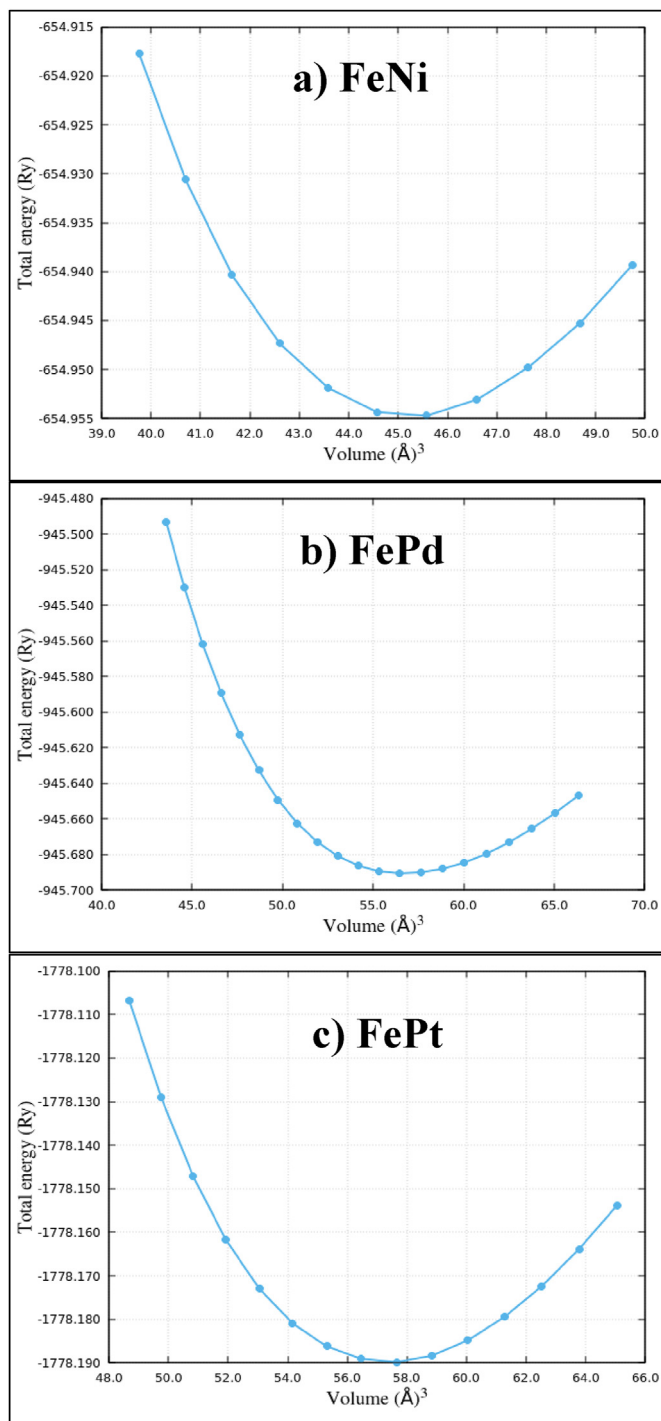

Figure 4. The total energy per unit cell as a function of the volume for a) FeNi, b) FePd, and c) FePt. The dots are the data points obtained from the PBE approximation. Solid line: Third-order Birch–Murnaghan equation of state fitting.

U presented in Table 2 were calculated for the elements used in this study using a technique proposed by Cococcioni [39]. Thus, enabling us to study the effect of onsite Coulomb interaction (U) under (GGA + U) and (LSDA + U) formulation of the DFT.

The Heisenberg exchange parameters were calculated using Green's functions formalism by adopting the method proposed by Korotin *et al.* [40]. In this case, a supercell of 16 atoms consisting of $2 \times 2 \times 2$ unit cells is considered, as shown in Figure 1b. The purpose of using supercell is to include all possible exchange interactions. Based on this structure, five

parameters are present: J_{Fe1}, J_{Fe2}, J_{FeM}, J_{M1}, and J_{M2}, where M indicates Ni, Pd, or Pt. These parameters are shown in Figure 3.

2. Results

2.1. Crystal structures & bulk modulus

The FeM (M = Ni, Pd, or Pt) alloys considered in this study are crystallized in a tetragonal L1$_0$ structure with space group No. 123 (P4/mmm) with two possible unit cells shown in Figure 1. The first unit cell is FCT (shown in Figure 1b) consist of four atoms: two Fe atoms occupy (0, 0, 0) and (½, ½, 0) positions, and two M atoms occupy (½, 0, ½) and (0, ½, ½) positions. The second unit cell is BCT (shown in Figure 1c) contains two atoms: Fe atom occupies (0, 0, 0) lattice site and M atom occupies (½, ½, ½) lattice site.

The lattice parameters for the FCT unit cell were calculated using different approximation methods for the three models shown in Figure 2. These models are antiferromagnetic (Model 1), ferrimagnetic (Model 2), and ferromagnetic (Model 3). The results for our calculations are shown in Table 1, alongside the corresponding experimental and theoretical values from the literature for comparison. The total energy differences between the considered models are shown in Table 2. Based on our results, the first-principles calculations for a complete lattice relaxation reveal that model 3 is the most stable configuration. This conclusion coincides with the experimental outcome from the literature [41]. Furthermore, the PBE approximation results are the closest to the cited experimental values. Thus, the lattice parameters of PBE will be used from hereafter.

For bulk modulus calculations, the total energy is calculated using PBE approximation at several points around the equilibrium volume. Then, these data will be fitted using the third-order Birch–Murnaghan equation of state [42], as shown in Figure 4. From the fitting data, the bulk modulus B_0 and its derivative for the ordered L1$_0$ FeNi, FePd, and FePt can be estimated as shown in Table 1. For FeNi as an example, our calculations yield $B_0 = 182.5$ GPa at 0K. This is very close to the range of the experimental values for Fe$_{0.5}$Ni$_{0.5}$ alloy at room temperature, which is expanding from 165 GPa to 177 GPa [42, 43].

2.2. Density of states

The tetrahedron method is used to calculate the total density of states (TDOS) and the partial density of states (PDOS) for the three configuration models: antiferromagnetic (Model 1), ferrimagnetic (Model 2), and ferromagnetic (Model 3), as illustrated in Figure 2. Our results are shown in Figure 5, where the spin-up density of states (DOS) is indicated by positive values, and negative values indicate spin-down (DOS) while the Fermi level is set to zero.

It is clear from Figure 5 (top three panels) that models 2 and 3 have very strong magnetic behavior due to the asymmetry between spin-up and spin-down TDOS. On the contrary, the symmetry of the TDOS in model 1 indicates a zero-sum of the total magnetic moment. Fermi energy slightly fluctuates among the studied alloys due to the small difference between the number of valence electrons for Ni, Pt, and Pd. For both FePd and FePt in Model 1 (AFM), an obvious deep minimum in the TDOS is present. Similarly, this minimum or "pseudogap" also occurs in the TDOS for FeNi in model 1 but is much weaker. For each alloy, this minimum is
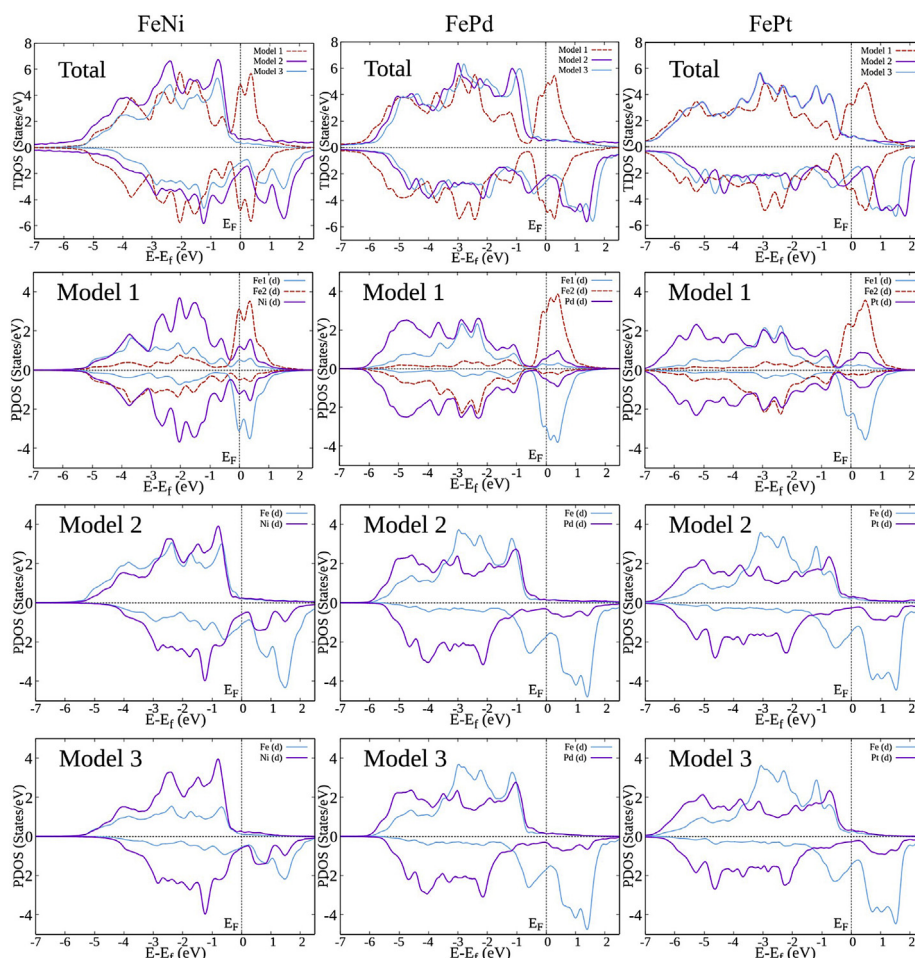

Figure 5. Total density of states (top panel) and projected density of states (bottom three panels) for each model of FeNi, FePd, and FePt. E$_F$ is the Fermi energy.

below Fermi energy. For models 2 and 3, the d-states (DOS) for Fe and M atoms (M = Ni, Pd, or Pt) noticeably overlap with each other. This occurs just below fermi energy in the majority spin states, indicating a strong hybridization between them.

2.3. Magnetic moment & magnetocrystalline anisotropy

The calculations of magnetocrystalline anisotropy (MCA) and Heisenberg exchange interaction parameters (J_{ij}) are very sensitive to the number of k-points. Thus, it is very important to choose enough k-points to sample the reciprocal space accurately. Figure 6 shows the convergence test for both MCA and J_{ij} for model 3 of the three different alloys used in this work. Based on the analysis of these data, the number of k-points in the first Brillouin zone needed for accurately estimating MCA and J_{ij} are 5832 and 5184, respectively. The difference between the number of k-points for MCA and J_{ij} is due to the difference in the c/a ratio. For MCA, we used an FCT structure with c/a ~0.95 corresponding to a sampling of $18 \times 18 \times 18$ k-points, while for J_{ij}, a BCT structure is used with c/a~ 1.35 corresponding to a sampling of 18*18*16 k-points.

To study the magnetocrystalline anisotropy for the three examined models, we considered the alignment of the magnetic moments along the directions [100], [110], and [001]. Our results are presented in Table 3 alongside the corresponding experimental data from the literature Focusing on model 3, which has the most stable configuration, we found that: MCA for FeNi is within the range of the reported experimental values, MCA for FePt is slightly above, and MCA for FePd is clearly beyond the reported experimental values.

Experimentally, due to the difficulty synthesizing perfectly ordered samples and the complexity in cooling the sample close to the absolute zero, the measured value of (MCA) tends to be always lower than the theoretical value [14, 48]., which is the case here. In addition, the orbital polarization correction was not considered in our calculations. This factor has been reported to increase the MCA even more [49, 50].

FePt alloy showed a significant magnetocrystalline anisotropy due to the large spin-orbit coupling of heavy Pt atom and a strong hybridization of the d bands of Pt and Fe [51], making spin-orbit interactions much stronger. On the other hand, for the FePd and FeNi alloys, the contribution of the relatively lighter atoms Pd and Ni is very small since the magnetocrystalline anisotropy mainly originates from orbital magnetic moments of Fe through spin-orbit interaction [52].

Furthermore, the atomic magnetic moment differences along the considered directions are very small (<0.01 μ_B/atom). Consequently, it is hard to specify the most energetically favorable direction for the alignment of the magnetic moment within the accuracy limit of our calculations.

2.4. Heisenberg exchange interaction

Finally, Table 4 shows the Heisenberg exchange interaction parameters (J_{ij}) for all models. Similar atoms display pronounced positive exchange interactions, indicating that Fe spins in each plane would prefer to align ferromagnetically. On the other hand, different atoms in model 2 show negative interaction parameters indicating that different atoms have opposite spin signs. The exchange interactions between atoms along
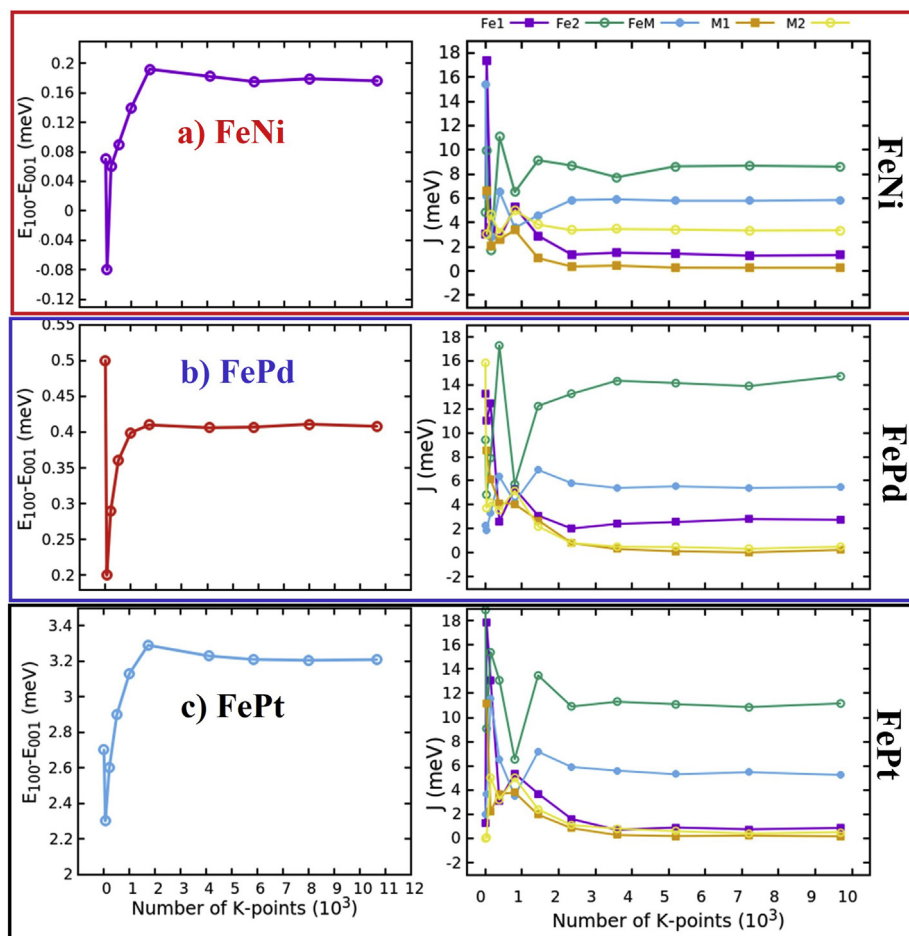

Figure 6. Convergence test for both magnetocrystalline anisotropy (MCA) (left panels) and Heisenberg exchange interaction (J) (right panels) for model 3 (FM) for a) FeNi, b) FePd, and c) FePt. E_{ijk} indicates the direction of the magnetic moments (including spin-orbit coupling).

Table 3. Total magnetic moments, the magnetic moment per atom, and magnetocrystalline anisotropy (MCA) corresponding to three possible directions ([100], [110], and [001]) for each model of the three considered models shown in Figure 2.

		M_{Fe} (μ_B/atom)	M_M (μ_B/atom)	M (μ_B/f.u.)	MCA GGA (meV/f.u.)	MCA GGA + U	
						(meV/f.u.)	(MJ/m³)
FeNi							
Model 1	001	2.34	0.0	0.0	0.015	0.128	0.89
	100	2.34	0.0				
	110	2.34	0.0				
Model 2	001	2.68	0.67	6.52	0.023	0.151	1.06
	100	2.68	0.68				
	110	2.67	0.68				
Model 3	001	2.67	0.68	6.52	0.053	0.181	1.27
	100	2.67	0.68				
	110	2.67	0.68				
Theor.		2.74 [53]	0.70 [53]		-	0.067 [53] 0.11 [54] 0.11 [12]	0.47 [53] 0.78 [54] 0.77 [12]
Exp.		2.6 ± 0.16 [55]	0.73 ± 0.0.4 [55]		-	-	0.58–1.3 [54,56]
FePd							
Model 1	001	2.88	0.0	0.0	0.092	0.241	1.69
	100	2.88	0.0				
	110	2.88	0.0				
Model 2	001	3.03	0.38	6.67	0.028	0.171	1.20
	100	3.03	0.38				
	110	3.02	0.38				
Model 3	001	3.02	0.38	6.65	0.016	0.417	2.92
	100	3.03	0.38				
	110	3.02	0.37				
Theor.		2.81 [57]	0.40 [57]	6.42 [57]	-	0.29 [58]	1.70 [58]
Exp.		3.01 [59]	0.30 [59]	6.62 [59]	-	-	1.5 [21], 2.1 [22]
FePt							
Model 1	001	2.88	0.0	0.0	0.41	1.62	11.33
	100	2.88	0.0				
	110	2.89	0.0				
Model 2	001	3.02	0.38	6.66	0.26	1.42	9.93
	100	3.02	0.37				
	110	3.02	0.38				
Model 3	001	3.02	0.38	6.67	1.73	3.203	22.42
	100	3.02	0.38				
	110	3.01	0.38				
Theor.		2.92 [60] 3.11 [61]	0.33 [60] 0.39 [61]	-	-	2.68 [61] 2.90 [60]	-
Exp.		-	-	-	-	1.9–3.16 [16,62,63]	-

the **b**-axis will be identical to the interactions along the **a**-axis since they share the same distances. The importance of calculating Heisenberg exchange interaction parameters is to calculate Curie temperature for these structures. Curie temperature can be calculated using many approaches, and the most popular one is using mean-field theory (MFT). However, this method suffers from a lack of accuracy. The alternate method is implementing Monte Carlo (MC) simulation, which is well known for its accuracy.

3. Conclusion

We have performed the first principals' calculations on L1$_0$-ordered FeNi, FePd, and FePt alloys in three different spin configurations. The structural, electronic, and magnetic properties were investigated. Structural properties such as lattice parameters, bulk modulus, and its derivative were computed by implementing several approximations for the exchange-correlation functional potentials. In this regard, the results of the PBE approximation proven to be the closest to the experimental values. We showed that ferromagnetic configuration is the most stable configuration for the considered alloys. For ferrimagnetic and ferromagnetic states, a strong hybridization between d orbits of the compound atoms is found below fermi energy in the majority spin states. For the antiferromagnetic state, a pseudogap is observed below fermi energy.

Table 4. Heisenberg exchange interaction parameters (meV) for model 1 (Antiferromagnetic), model 2 (Ferrimagnetic), and model 3 (Ferromagnetic).

		J_{Fe1}	J_{Fe2}	J_{M1}	J_{M2}	J_{FeM}
FeNi	Model 1 (AFM)	0.849	-8.157	0.216	2.671	5.581
	Model 2 (FIM)	0.573	7.291	0.161	3.223	-5.352
	Model 3 (FM)	1.419	8.631	0.261	3.416	5.785
FePd	Model 1 (AFM)	1.927	-15.478	0.241	0.492	5.918
	Model 2 (FIM)	2.052	14.359	0.088	0.553	-5.431
	Model 3 (FM)	2.551	14.352	0.302	0.504	5.401
FePt	Model 1 (AFM)	1.824	-13.734	0.011	0.581	5.475
	Model 2 (FIM)	4.056	12.642	0.999	0.296	-6.638
	Model 3 (FM)	0.903	11.101	0.193	0.602	5.304

Magnetocrystalline anisotropy (MCA) is calculated for each alloy in all spin configurations. FePt alloy showed an exceptionally large MCA value in the order of 3 meV/f.u. Finally, we calculated Heisenberg exchange interaction parameters for ferrimagnetic and ferromagnetic states. These parameters can be utilized for further studies using Monte-Carlo simulations.

Declarations

Author contribution statement

K. Aledealat: Analyzed and interpreted the data; Wrote the paper.
B. Aladerah: Performed the experiments.
A. Obeidat: Conceived and designed the experiments.
M. Gharaibeh: Analyzed and interpreted the data.

Funding statement

Data availability statement

Data will be made available on request.

Declaration of interests statement

The authors declare no conflict of interest.

Additional information

No additional information is available for this paper.

References

[1] M. Futamoto, et al., Growth of L10-ordered crystal in FePt and FePd thin films on MgO(001) substrate, AIP Adv. 6 (8) (2016) 85302.
[2] K.M. Krishnan, et al., Exchange biasing of permalloy films by MnxPt1−x: role of composition and microstructure, J. Appl. Phys. 83 (11) (1998) 6810–6812.
[3] S.C. Tsang, et al., Assembly of centimeter long silica coated FePt colloid crystals with tailored interstices by magnetic crystallization, Chem. Mater. 20 (14) (2008) 4554–4556.
[4] K.M. Krishnan, et al., Nanomagnetism and spin electronics: materials, microstructure and novel properties, J. Mater. Sci. 41 (3) (2006) 793–815.
[5] I. Koh, L. Josephson, Magnetic nanoparticle sensors, Sensors 9 (10) (2009) 8130–8145.
[6] T.A.P. Rocha-Santos, Sensors and biosensors based on magnetic nanoparticles, Trac. Trends Anal. Chem. 62 (2014) 28–36.
[7] M. Neamtu, et al., Functionalized magnetic nanoparticles: synthesis, characterization, catalytic application and assessment of toxicity, Sci. Rep. 8 (1) (2018) 6278.
[8] T.S. Rodrigues, A.G.M. da Silva, P.H.C. Camargo, Nanocatalysis by noble metal nanoparticles: controlled synthesis for the optimization and understanding of activities, J. Mater. Chem. 7 (11) (2019) 5857–5874.
[9] L.M. Rossi, et al., Magnetic nanomaterials in catalysis: advanced catalysts for magnetic separation and beyond, Green Chem. 16 (6) (2014) 2906–2933.
[10] R. Ferrando, J. Jellinek, R.L. Johnston, Nanoalloys:From theory to applications of alloy clusters and nanoparticles, Chem. Rev. 108 (3) (2008) 845–910.
[11] S. Singamaneni, et al., Magnetic nanoparticles: recent advances in synthesis, self-assembly and applications, J. Mater. Chem. 21 (42) (2011) 16819–16845.
[12] A. Edström, et al., Electronic structure and magnetic properties of L 1 0 binary alloys, Phys. Rev. B 90 (1) (2014) 14402.
[13] P. Bruno, Tight-binding approach to the orbital magnetic moment and magnetocrystalline anisotropy of transition-metal monolayers, Phys. Rev. B 39 (1) (1989) 865–868.
[14] Y. Kota, A. Sakuma, Relationship between magnetocrystalline anisotropy and orbital magnetic moment in L10-type ordered and disordered alloys, J. Phys. Soc. Jpn. 81 (8) (2012) 84705.
[15] H.J.F. Jansen, Magnetic anisotropy in density-functional theory, Phys. Rev. B 38 (12) (1988) 8022–8029.
[16] K. Barmak, et al., On the relationship of magnetocrystalline anisotropy and stoichiometry in epitaxial L10 CoPt (001) and FePt (001) thin films, J. Appl. Phys. 98 (3) (2005) 33904.
[17] R.F.C. Farrow, et al., Control of the axis of chemical ordering and magnetic anisotropy in epitaxial FePt films, J. Appl. Phys. 79 (8) (1996) 5967–5969.
[18] H. Kanazawa, G. Lauhoff, T. Suzuki, Magnetic and structural properties of (CoxFe100−x)50Pt50 alloy thin films, J. Appl. Phys. 87 (9) (2000) 6143–6145.
[19] S. Okamoto, et al., Chemical-order-dependent magnetic anisotropy and exchange stiffness constant of FePt (001) epitaxial films, Phys. Rev. B 66 (2) (2002) 24413.
[20] T. Shima, et al., Low-temperature fabrication of L10 ordered FePt alloy by alternate monatomic layer deposition, Appl. Phys. Lett. 80 (2) (2002) 288–290.
[21] V. Gehanno, et al., Magnetic domains in epitaxial ordered FePd(001) thin films with perpendicular magnetic anisotropy, Phys. Rev. B 55 (18) (1997) 12552–12555.
[22] H. Shima, et al., Lattice axial ratio and large uniaxial magnetocrystalline anisotropy in $L{1}_{0}$-type FePd single crystals prepared under compressive stress, Phys. Rev. B 70 (22) (2004) 224408.
[23] M. Kotsugi, et al., Origin of strong magnetic anisotropy in L10-FeNi probed by angular-dependent magnetic circular dichroism, J. Magn. Magn Mater. 326 (2013) 235–239.
[24] L. Néel, et al., Magnetic properties of an iron—nickel single crystal ordered by neutron bombardment, J. Appl. Phys. 35 (3) (1964) 873–876.
[25] G. Brown, et al., Competition between ferromagnetism and antiferromagnetism in FePt, Phys. Rev. B 68 (5) (2003) 52405.
[26] I. Shuttleworth, The magnetic band-structures of ordered PtxFe1−x, PtxCo1−x, and PtxNi1−x (x = 0.25, 0.50, and 0.75), Magnetochemistry 6 (1) (2020) 61.
[27] M. Werwiński, W. Marciniak, Ab initio study of magnetocrystalline anisotropy, magnetostriction, and Fermi surface of L10 FeNi (tetrataenite), J. Phys. D Appl. Phys. 50 495008 (2017) 50.
[28] E. Burzo, P. Vlaic, Magnetic properties of iron-palladium solid solutions and compounds, J. Optoelectron. Adv. Mater. 12 (2010) 1869–1878.
[29] P. Hohenberg, W. Kohn, Inhomogeneous electron gas, Phys. Rev. 136 (3B) (1964) B864–B871.
[30] W. Kohn, L.J. Sham, Self-consistent equations including exchange and correlation effects, Phys. Rev. 140 (4A) (1965) A1133–A1138.
[31] P.E. Blöchl, Projector augmented-wave method, Phys. Rev. B 50 (24) (1994) 17953–17979.
[32] G. Kresse, D. Joubert, From ultrasoft pseudopotentials to the projector augmented-wave method, Phys. Rev. B 59 (3) (1999) 1758–1775.
[33] D. Vanderbilt, Soft self-consistent pseudopotentials in a generalized eigenvalue formalism, Phys. Rev. B 41 (11) (1990) 7892–7895.
[34] J.P. Perdew, A. Zunger, Self-interaction correction to density-functional approximations for many-electron systems, Phys. Rev. B 23 (10) (1981) 5048–5079.
[35] J.P. Perdew, K. Burke, M. Ernzerhof, Generalized gradient approximation made simple, Phys. Rev. Lett. 77 (18) (1996) 3865–3868.
[36] J.P. Perdew, Y. Wang, Accurate and simple analytic representation of the electron-gas correlation energy, Phys. Rev. B 45 (23) (1992) 13244–13249.
[37] J.P. Perdew, et al., Restoring the density-gradient expansion for exchange in solids and surfaces, Phys. Rev. Lett. 100 (13) (2008) 136406.
[38] S.L. Dudarev, et al., Electron-energy-loss spectra and the structural stability of nickel oxide: an LSDA+U study, Phys. Rev. B 57 (3) (1998) 1505–1509.
[39] M. Cococcioni, S. de Gironcoli, Linear response approach to the calculation of the effective interaction parameters in the $\\mathrm{LDA}+\\mathrm{U}$ method, Phys. Rev. B 71 (3) (2005) 35105.
[40] D.M. Korotin, et al., Calculation of exchange constants of the Heisenberg model in plane-wave-based methods using the Green's function approach, Phys. Rev. B 91 (22) (2015) 224405.
[41] R. Wirths, P. Runow, H. Schöpgens, Magnetic study of the ordered and quenched equiatomic FePt alloy, Phys. Status Solidi 33 (1) (1976) 135–142.
[42] M. Werwiński, W. Marciniak, Ab initiostudy of magnetocrystalline anisotropy, magnetostriction, and Fermi surface of L10FeNi (tetrataenite), J. Phys. Appl. Phys. 50 (49) (2017) 495008.
[43] Bonnenberg, D., K.A. Hempel, and H.P.J. Wijn, 1.2.1.2.9 Magnetomechanical Properties, Elastic Moduli, Sound Velocity: Datasheet from Landolt-Börnstein - Group III Condensed Matter · Volume 19A: "3d, 4d and 5d Elements, Alloys and Compounds" in SpringerMaterials H.P.J. Wijn, Editor, Springer-Verlag Berlin Heidelberg.
[44] A. Frisk, et al., Strain engineering for controlled growth of thin-film FeNi L10. Strain Engineering for Controlled Growth of Thin-Film FeNi L10, 2017, p. 50.
[45] P. Villars, P. Villars, Pearson's Handbook : Crystallographic Data for Intermetallic Phases, Materials Park, OH: ASM International, 1997.
[46] M. Sternik, et al., Dynamical properties of ordered Fe–Pt alloys, J. Alloys Compd. 651 (2015) 528–536.
[47] Metals Handbook, American Society for Metals, Matals Park, Ohio, 1985.
[48] J. Staunton, et al., Long-range chemical order effects upon the magnetic anisotropy of FePt alloys from an ab initio electronic structure theory, J. Phys. Condens. Matter 16 (48) (2004) S5623.
[49] P. Ravindran, et al., Large magnetocrystalline anisotropy in bilayer transition metal phases from first-principles full-potential calculations, Phys. Rev. B 63 (14) (2001) 144409.
[50] Y. Miura, et al., The origin of perpendicular magneto-crystalline anisotropy in L10–FeNi under tetragonal distortion, J. Phys. Condens. Matter 25 (10) (2013) 106005.
[51] A. Sakuma, First principle calculation of the magnetocrystalline anisotropy energy of FePt and CoPt ordered alloys, J. Phys. Soc. Jpn. 63 (8) (1994) 3053–3058.
[52] M. Kumar, V. Verma, V. Singh, Magnetic anisotropic of thermally evaporated FeNi thin film: a soft X-ray magnetic circular dichroism study, Surf. Interface Anal. 53 (9) (2021) 808–813.

[53] M. Werwiński, W. Marciniak, Ab initio study of magnetocrystalline anisotropy, magnetostriction, and Fermi surface of L10 FeNi (tetrataenite), J. Phys. Appl. Phys. 50 (49) (2017) 495008.

[54] L.H. Lewis, et al., De magnete et meteorite: cosmically motivated materials, IEEE Magn. Lett. 5 (2014) 1–4.

[55] J.W. Cable, E.O. Wollan, Magnetic-moment distribution in NiFe and AuFe alloys, Phys. Rev. B 7 (5) (1973) 2005–2016.

[56] M. Mizuguchi, et al., Artificial fabrication and order parameter estimation of L10-ordered FeNi thin film grown on a AuNi buffer layer, J. Magn. Soc. Jpn. 35 (4) (2011) 370–373.

[57] E. Burzo, P. Vlaic, Magnetic properties of iron-palladium solid solutions and compounds, J. Optoelectron. Adv. Mater. 12 (9) (2010) 1869.

[58] Y. Kota, A. Sakuma, Mechanism of uniaxial magnetocrystalline anisotropy in transition metal alloys, J. Phys. Soc. Jpn. 83 (3) (2014) 34715.

[59] J. Lyubina, O. Gutfleisch, O. Isnard, Phase transformations and magnetic structure of nanocrystalline Fe–Pd and Co–Pt alloys studied by in situ neutron powder diffraction, J. Appl. Phys. 105 (7) (2009) 7A717.

[60] Z. Lu, R.V. Chepulskii, W. Butler, First-principles study of magnetic properties of L 1 0-ordered MnPt and FePt alloys, Phys. Rev. B 81 (9) (2010) 94437.

[61] A.B. Shick, O.N. Mryasov, Coulomb correlations and magnetic anisotropy in ordered L 1 0 CoPt and FePt alloys, Phys. Rev. B 67 (17) (2003) 172407.

[62] J.P. Liu, et al., High energy products in rapidly annealed nanoscale Fe/Pt multilayers, Appl. Phys. Lett. 72 (4) (1998) 483–485.

[63] A. Deák, et al., Metallic magnetism at finite temperatures studied by relativistic disordered moment description: theory and applications, Phys. Rev. B 89 (22) (2014) 224401.